



Fabrication of silicon-based porous nanocomposite films by focused infrared light sintering

Jiwang Yan (2)*, Kouga Okada

Department of Mechanical Engineering, Keio University, Yokohama 223-8522, Japan



ARTICLE INFO

Keywords:
Sintering
Composite
Silicon

ABSTRACT

A beam of focused infrared light was used to sinter a mixture of silicon powders, copper nanoparticles, and carbon nanotubes for fabricating porous nanocomposite films. Copper was preferentially heated by the infrared light, while silicon was indirectly heated through heat conduction because of its transparency to infrared light. Micro wire formation and interfacial element diffusion were detected on the sintered film surfaces. Networks of copper binder and carbon nanotubes, which provide high binding strength and electrical conductivity, were successfully generated. The sintered depth, porosity rate, and silicon crystallinity were controllable by varying the scan speed of the infrared light.

© 2016 CIRP.

1. Introduction

Additive manufacturing (AM) has received focus in recent years from multidisciplinary fields [1–3]. Currently, plastics, metals, ceramics, and their composites are major materials used for AM [4–7]. However, there is minimal literature on the AM of silicon-based composites even if they have a wide range of important applications. For example, silicon-based porous nanocomposites and silicon sponges are excellent substrates for fabricating high-performance lithium ion batteries [8–10].

In this study, a new sintering system is developed using a beam of focused infrared light to sinter a mixture of silicon (Si) powders, copper (Cu) nanoparticles, and carbon nanotubes (CNTs). The proposed method enables mild sintering of silicon-based porous nanocomposite films with high bending strength and electrical conductivity. The surface/interface phenomena, material structural transformations, and porosity changes during sintering are investigated experimentally. The mechanical and electrical properties of the sintered films are also evaluated.

2. Mechanism for focused infrared light sintering

As schematically illustrated in Fig. 1, Si is transparent in the infrared region and is not heated directly by infrared light. Conversely, Cu absorbs infrared rays efficiently and is preferentially heated. The melting and resolidification of Cu leads to a strong binder between Si grains. Simultaneously, heat conduction from Cu to Si occurs, which indirectly heats the Si grains at their interfaces. The degree of Si melting is dependent upon the intensity and scan speed of the infrared light, which may be used to control the sintered depth, porosity, and crystallinity of the Si. CNTs have

high thermal stability and low absorption of infrared light and thus are less influenced during sintering. However, CNTs can generate a conductive network in the composite by bridging the resolidified Cu binders.

In conventional laser sintering, the outmost layer of material is intensively processed at an extremely high temperature gradient [11] and the laser pulses cause scattering of the nanoparticles. Conversely, the infrared light can penetrate deeply into material without pulse impacts, enabling stable and mild sintering of a thick layer of material at a low temperature gradient. Thus, the scattering of nanoparticles can be prevented and the pores among the particles can be retained. Furthermore, compared with infrared furnaces, a beam of infrared light enables selective sintering, with less thermal damage to the supporting substrate.

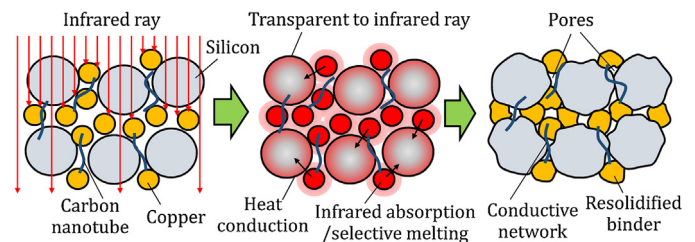


Fig. 1. Model for infrared sintering of Si/Cu/CNT nanocomposite.

3. Experimental procedures

A prototype sintering system was constructed as presented in Fig. 2(a). An infrared light generator was installed on an XYZ three-axis stage. The XY tables enable the infrared light beam to scan over a maximum area of 200 mm × 200 mm; the Z slide is used to adjust the height of the infrared light generator. Fig. 2(b) is a schematic of the infrared light generator. The infrared light (wavelength 1 μm) generated by an infrared lamp is concentrated by an ellipsoidal

* Corresponding author. Tel.: +81 455661445.
E-mail address: yan@mech.keio.ac.jp (J. Yan).

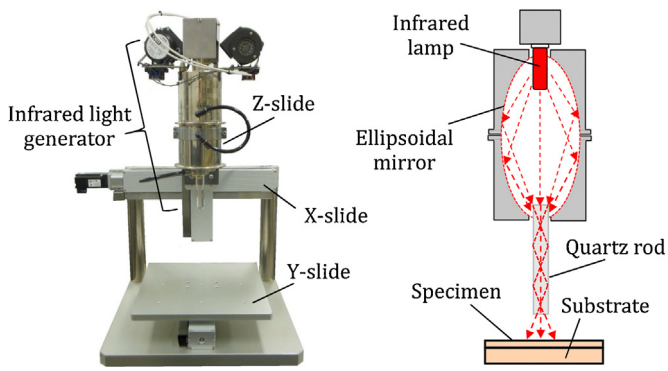


Fig. 2. Photograph and schematic of developed experimental setup.

mirror and focused to the upper end of a quartz rod that has a diameter of 20 mm. The light beam is then led out by the quartz rod via the total internal reflection effect. Consequently, a focused infrared light beam is irradiated onto the specimen surface. In this study, the electrical current input to the infrared light generator was fixed at 20 A. Fig. 3 displays plots of the temperature distributions of a heated carbon plate measured by a noncontact infrared temperature sensor. The temperature changes with the radial distance (x) from the light beam center and the vertical distance (z) between the specimen surface and the end of the quartz rod. The highest temperature in this case is 1030 °C (when sintering the composite, the temperature will be much higher). Sintering was performed in air and argon gas.

A mixture of Si powders, Cu nanoparticles, and CNTs was used as a specimen. Rather than using expensive pure Si nanoparticles, we used waste Si powder from a wire saw slicing process for Si wafers in the manufacturing of solar cells and semiconductor devices [10]. As can be observed in Fig. 4(a), the waste Si powder ranged in size from a number of sub-microns to several microns. Cu nanoparticles with a mean size of 200 nm (melting point 1085 °C), as presented in Fig. 4(b), and CNTs with a diameter of 10–20 nm and length 0.1–10 μm were added to the Si powder at various mass ratios. The mixture was agitated by a ball mill to obtain a slurry into which N-methylpyrrolidone was added as an organic solvent. The slurry was then applied to a 100–300 μm -thick Cu substrate and dried at 100 °C before sintering. The sintered

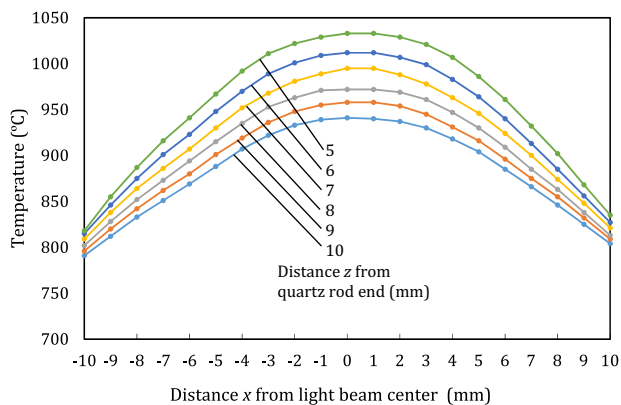


Fig. 3. Temperature plots on an infrared light-irradiated carbon plate.

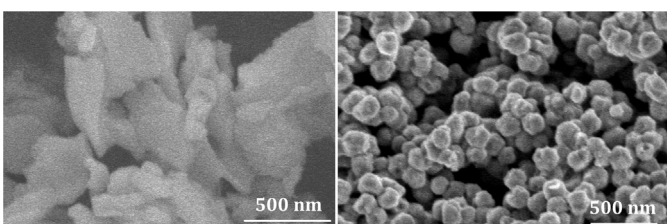


Fig. 4. SEM images of (a) Si powders and (b) Cu nanoparticles.

composite film thickness ranged from 20 μm to 200 μm . The films were analyzed using scanning electron microscopy (SEM) equipped with energy dispersive X-ray spectroscopy (EDX). The crystallinity of the Si was characterized by Raman spectroscopy.

4. Results and discussion

4.1. Surface/interface phenomena

Fig. 5 displays typical SEM images of sintered composite surfaces. As can be observed in Fig. 5(a), where mass ratio Si:Cu = 2:1, $z = 5$ mm, and light beam scan speed $v = 2.0$ mm/s, the Si powders have been melted, rounded, and merged forming a continuous body. Interestingly, a number of Si micro wires were formed protruding from the film surface. Fig. 5(b) is another example obtained at $z = 1$ mm and $v = 0.2$ mm/s. In this example, the sintered film surface is covered densely by Si micro wires. The formation of Si micro wires could be a consequence of continuous heating, which caused melting and regrowth of Si. Micro wires significantly increase the effective surface area and absorption rate of electrolyte fluid, thus improve the performance of lithium ion batteries. Fig. 6 is an SEM image of a sintered film surface at $z = 5$ mm and $v = 0.5$ mm/s and its corresponding EDX result. Though some Cu nanoparticles retained their original size (~ 200 nm), clusters of much finer nanoparticles (~ 50 nm) were generated and the surface beneath these particle clusters indicates a color change and EDX responses for both Cu and Si. This result indicates that element diffusion or a chemical reaction between the Cu and Si could have occurred, which is similar to the chemically induced binding in laser sintering [5].

4.2. Cross-sectional observation

Fig. 7 is a cross-sectional SEM image of a sintered film at $z = 5$ mm and $v = 2.0$ mm/s. Two layers with different structures

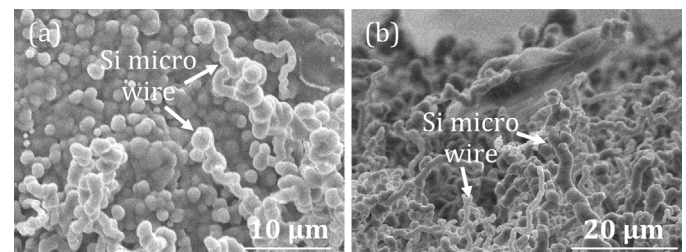


Fig. 5. SEM images of sintered film surfaces with Si micro wires.

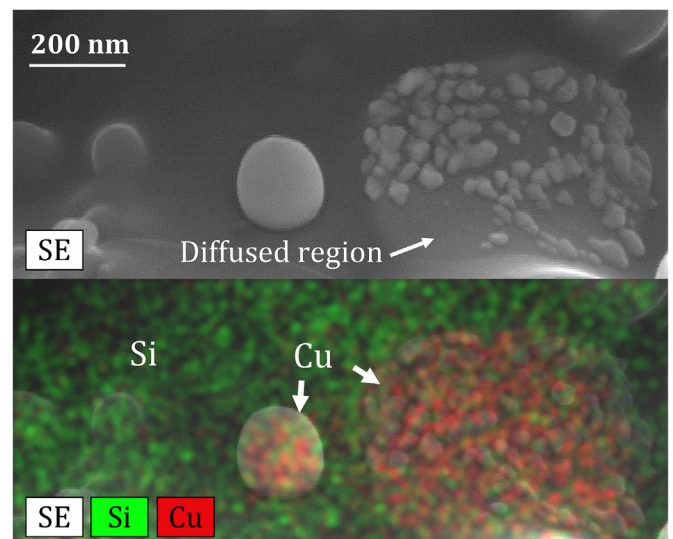


Fig. 6. SEM/EDX of sintered film surfaces with Cu diffusion.

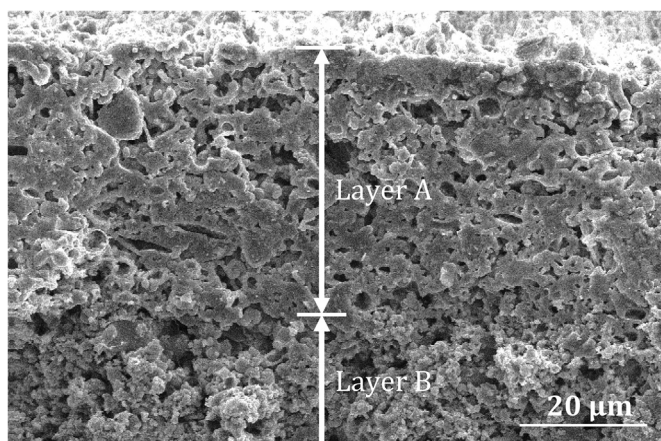


Fig. 7. Cross-sectional SEM image of a sintered composite film.

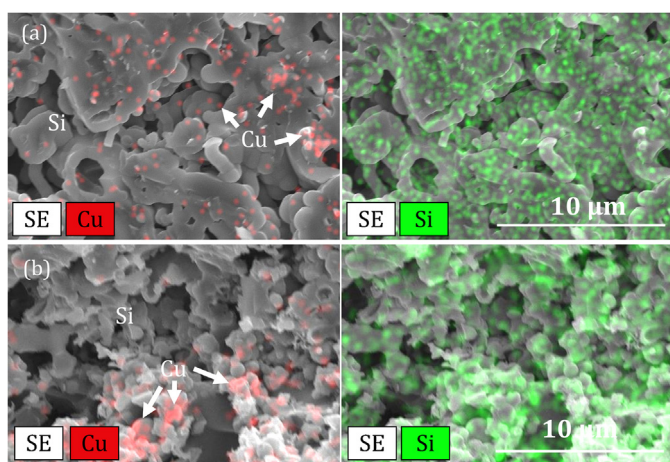


Fig. 8. Magnified SEM images with EDX mapping of layers A and B in Fig. 7.

are identified: a fully sintered layer A on top and a partially sintered layer B beneath layer A. Fig. 8(a) is a pair of SEM images of layer A with EDX mapping. In this layer, the Si has been significantly melted and resolidified into a porous continuous body, like a sponge, dotted with Cu particles. Fig. 8(b) is the counterpart of layer B. In layer B, the Si powders were not fully melted, rather bonded together by the partially melted Cu binder, leaving a granular structure with micro pores.

4.3. Change of sintered depth

Fig. 9 illustrates the change of depth of the fully sintered layer A with the scan speed of infrared light beam. As a general trend, the

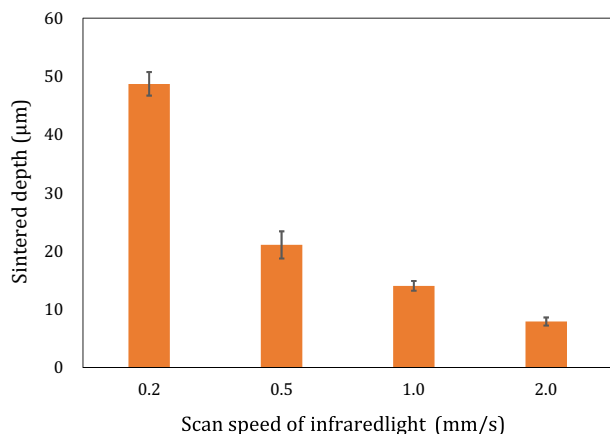


Fig. 9. Change of sintered depth with scan speed of infrared light.

sintered depth decreased with an increase of the light beam scan speed. When the light beam scanned rapidly, the Cu nanoparticles in the deep region were heated by the infrared light and melted; however, heat conduction from Cu to Si was insufficient to cause Si melting. When the light beam scanned slowly, the heat conduction in the top layer was sufficiently significant to cause extensive Si melting. The melted Si had a higher absorption rate of infrared light and less heat was delivered to the deeper region. The results in Fig. 9 are important for optimizing sintering conditions for a specific film thickness. It is also noteworthy that the sintered depth per scan of infrared light beam is $\sim 50 \mu\text{m}$, remarkably greater than that reported in laser sintering.

4.4. Porosity change

Fig. 10 indicates the change in porosity of the fully sintered layer A with the scan speed of infrared light. The porosity was measured by processing cross-sectional SEM images using the Image-J software. In Fig. 10, clearly the porosity decreased as the scan speed of the infrared light decreased. When the light beam scanned slowly, the heat conduction in the top layer was sufficient to melt and merge the Si grains leading to a decrease of porosity. Optimized porosity is important to suppress the significant volume change of a Si-based electrode for a lithium ion battery caused by charge/discharge cycles [8–10].

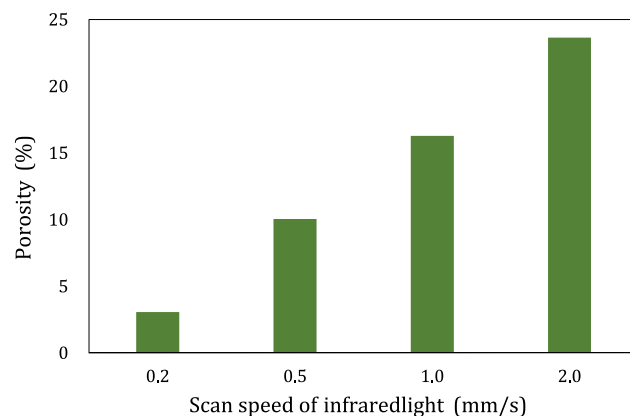


Fig. 10. Change of porosity of sintered film with infrared light scan speed.

4.5. Silicon crystallinity characterization

The crystallinity of Si in the sintered film was analyzed by laser Raman spectroscopy. In Raman spectra, a peak shift to the low-wave-number side indicates reduced crystallinity. As indicated in Fig. 11, the waste Si powder before infrared sintering had a peak at 514 cm^{-1} indicating a polycrystalline or highly strained structure caused by the wire saw slicing process. After sintering under conditions $z = 5 \text{ mm}$ and $v = 0.5 \text{ mm/s}$, the film had transitioned to a structure close to that of single-crystal Si (520 cm^{-1}). The improved crystallinity could be a consequence of melting and recrystallization of the Si powder during sintering, which greatly reduced the defects and phase transformations of Si that occurred in the slicing processes due to the extremely high pressure and shear stress [12].

4.6. Bending strength test

To evaluate the strength of the sintered composite films, bending tests were performed by wrapping the films around steel rods with different diameters ($d = 10\text{--}40 \text{ mm}$). Fig. 12 displays bent composite films sintered at different scan speeds of infrared light. In Fig. 12(a), a long crack is visible in the curved section of the film; whereas in Fig. 12(b), no crack is observed. Fig. 13 indicates the change of critical bending angle (θ_c) for crack generation at

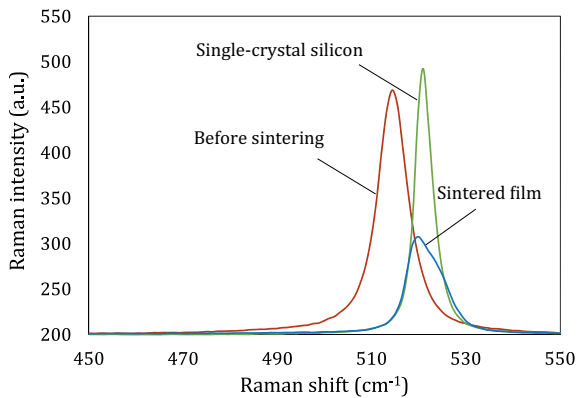


Fig. 11. Raman spectra of Si before and after sintering.



Fig. 12. (a) $v = 10.0$ mm/s; (b) $v = 0.5$ mm/s. Photographs of sintered composite films after bending tests.

$d = 40$ mm when the infrared light beam was scanned at various speeds. It is clear that the critical bending angle increased as the light beam scan speed decreased. Further, for all sintered films, the critical bending angles were greater than that of the film without sintering. It was also determined that the critical bending angle increased with the concentration of Cu nanoparticles and did not obviously change with that of the CNTs.

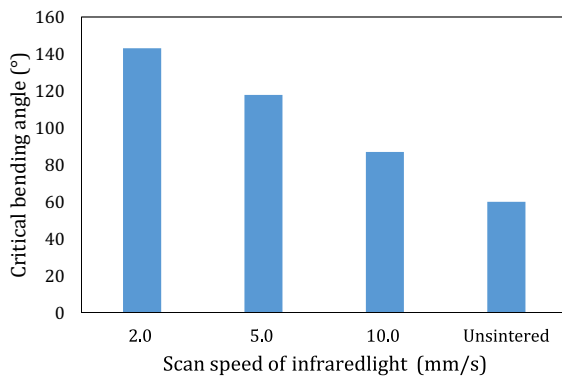


Fig. 13. Change of critical bending angle with scan speed of infrared light.

4.7. Electrical conductivity evaluation

Electrical conductivity is important for electrodes of lithium ion batteries. The electrical conductivity of composite films sintered under various conditions was measured. Fig. 14 illustrates the change of electrical conductivity with concentration ratio in mass of Si powder, Cu nanoparticles, and CNTs, in air and in argon gas environments. It is indicated that electrical conductivity was significantly improved by increasing the concentration of CNTs; whereas less influenced by that of the Cu nanoparticles. The conductivity of the films sintered in air was lower than those sintered in argon gas, which could be caused by the oxidation of the

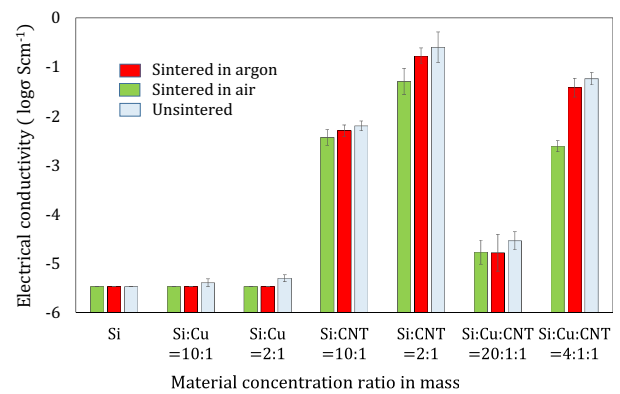


Fig. 14. Change of electrical conductivity of sintered films with material concentration ratios in mass and gas environments.

materials in air. It is noteworthy that after sintering, even in argon gas, the electrical conductivity of the films reduced slightly compared with the unsintered films. This could be caused by the micro Si wires generated on the film surface after sintering (Fig. 5), which blocked the CNTs from protruding from the film surface.

As future tasks, the fabrication of multilayered nanocomposites by infrared sintering will be attempted and the possibility of sintering other Si/metal nanocomposites will be investigated.

5. Conclusions

Focused infrared light was used to sinter a mixture of silicon powders, copper nanoparticles, and carbon nanotubes. Copper was preferentially heated by the infrared light; silicon was heated indirectly via heat conduction from copper, which enabled mild sintering of a nanocomposite film. Interesting phenomena such as micro wire generation, pore formation, interfacial element diffusion, and crystallinity change were discovered. It was determined that the sintered depth, porosity rate, and bending strength of the sintered films were controllable by varying the scan speed of the infrared light. Carbon nanotubes significantly improve the electrical conductivity of the sintered nanocomposite films, which is useful for electrode fabrication for future batteries.

References

- [1] Kruth JP, Leu MC, Nakagawa T (1998) Progress in Additive Manufacturing and Rapid Prototyping. *Annals of the CIRP* 47(2):525–540.
- [2] Bartolo P, Kruth JP, Silva J, Levy G, Malshe A, Rajurkar K, Mitsuishi M, Ciurana J, Leu M (2012) Biomedical Production of Implants by Additive Electro-Chemical and Physical Processes. *Annals of the CIRP* 61(2):635–655.
- [3] Huis in't Veld B, Overmeyer L, Schmidt M, Wegener K, Malshe A, Bartolo P (2015) Micro Additive Manufacturing Using Ultra Short Laser Pulses. *Annals of the CIRP* 64(2):701–724.
- [4] Hon KKB, Gill TJ (2003) Selective Laser Sintering of SiC/Polyamide Composites. *Annals of the CIRP* 52(1):173–176.
- [5] Kruth JP, Levy G, Klocke F, Childs THC (2007) Consolidation Phenomena in Laser and Powder-Bed Based Layered Manufacturing. *Annals of the CIRP* 56(2):730–759.
- [6] Overmeyer L, Neumeister A, Kling R (2011) Direct Precision Manufacturing of Three-Dimensional Components Using Organically Modified Ceramics. *Annals of the CIRP* 60(1):267–270.
- [7] Deckers J, Kruth JP, Shahzad K, Vleugels J (2012) Density Improvement of Alumina Parts Produced Through Selective Laser Sintering of Alumina-Polyamide Composite Powder. *Annals of the CIRP* 61(1):211–214.
- [8] Gowda SR, Pushparaj V, Herle S, Girishkumar G, Gordon JG, Gullapalli H, Zhan X, Ajayan PM, Reddy ALM (2012) Three-Dimensionally Engineered Porous Silicon Electrodes for Li Ion Batteries. *Nano Letters* 12(12):6060–6065.
- [9] Iwabuchi Y, Yan J (2015) Laser Sintering of Silicon Powder and Carbon Nanofibers for Porous Composite Thick Films. *Applied Physics Express* 8:026501.
- [10] Li X, Gu M, Hu S, Kennard R, Yan P, Chen X, Wang C, Sailor MJ, Zhang JG, Liu J (2014) Mesoporous Silicon Sponge as an Anti-Pulverization Structure for High-Performance Lithium-Ion Battery Anodes. *Nature Communications* 5:4105.
- [11] Zaeh MF, Ott M (2011) Investigations on Heat Regulation of Additive Manufacturing Processes for Metal Structures. *Annals of the CIRP* 60(1):259–262.
- [12] Yan J, Asami T, Harada H, Kuriyagawa T (2009) Fundamental Investigation of Subsurface Damage in Single Crystalline Silicon Caused by Diamond Machining. *Precision Engineering* 33(4):378–386.